Acta Crystallographica Section D
Biological Crystallography
ISSN 0907-4449

Human apolipoprotein A-I: structure determination and analysis of unusual diffraction characteristics

David W. Borhani,[a,b]* Jeffrey A. Engler[b] and Christie G. Brouillette[b,c]

[a]Department of Organic Chemistry, Southern Research Institute, Birmingham, AL 35205, USA, [b]Department of Biochemistry and Molecular Genetics, University of Alabama Medical Center, Birmingham, AL 35294, USA, and [c]Center for Macromolecular Crystallography, University of Alabama Medical Center, Birmingham, AL 35294, USA

Correspondence e-mail: borhani@sri.org

Received 10 June 1999
Accepted 14 October 1999

The crystallization and structure determination of recombinant human apolipoprotein A-I (apo A-I), the major protein component of high-density lipoprotein, is described. The fragment crystallized, residues 44–243 of native apo A-I [apo Δ(1–43)A-I], is very similar to intact native apo A-I in its ability to bind lipid, to be incorporated into high-density lipoproteins and to activate lecithin–cholesterol acyl transferase. Apo Δ(1–43)A-I crystallizes from 1.0–1.4 *M* sodium citrate pH 6.5–7.5 in space group $P2_12_12_1$, with unit-cell parameters $a = 97.47$, $b = 113.87$, $c = 196.19$ Å (crystal form I). The crystals exhibit unusual diffraction intensity spikes and axial extinctions that are discussed in the context of the 4 Å crystal structure. When flash-cooled to 100 K, the crystals diffract synchrotron radiation to 3 Å resolution. Radiation sensitivity and crystal-to-crystal variation have hindered the assembly of a complete 3 Å data set.

1. Introduction

Apolipoprotein A-I (apo A-I) is the major protein component of high-density lipoprotein (HDL). High blood levels of HDL strongly correlate with a reduced risk of atherosclerosis and hence a reduced risk of coronary artery disease (Catapano *et al.*, 1993; Castelli *et al.*, 1986; Gordon *et al.*, 1977; Miller *et al.*, 1977). Apo A-I plays several key roles in a major metabolic function of HDL: the reverse transport of cholesterol from peripheral tissues to the liver for catabolism (Miller, 1989; Rothblat *et al.*, 1992). It binds phospholipids to form discoidal HDL; it promotes the reversible efflux of cholesterol from peripheral cell plasma membranes into HDL; it activates lecithin–cholesterol acyl transferase (LCAT), the enzyme which traps cholesterol within HDL by converting cholesterol to cholesterol esters, thereby transforming immature discoidal HDL into mature spherical HDL; it is responsible for the recognition of HDL by the liver HDL receptor SR-BI (Acton *et al.*, 1993; Plump *et al.*, 1996; Kozarsky *et al.*, 1997; Rigotti *et al.*, 1997). A deeper understanding of how apo A-I facilitates these processes would be provided, in part, by the appropriate crystal structures of lipid-free and lipid-bound apo A-I.

We recently reported the first crystal structure of apo A-I (Borhani *et al.*, 1997). Our studies used an N-terminal truncation mutant of human apo A-I, 'apo Δ(1–43)A-I' (residues 44–243), that is very similar to native apo A-I (residues 1–243) in its ability to be incorporated into HDL and to activate LCAT (Rogers *et al.*, 1997). The properties of lipid-free apo Δ(1–43)A-I are distinct, however, from those of lipid-free apo A-I. In particular, loss of the N-terminus causes the C-terminus to adopt the ordered α-helical conformation characteristic of lipid-bound apo A-I (Rogers *et al.*, 1997). Therefore, the properties of lipid-free apo Δ(1–43)A-I mimic

those of lipid-bound apo A-I. This fact gave us the confidence to construct models of discoidal and spherical HDL from the lipid-free crystal structure of apo Δ(1–43)A-I (Borhani *et al.*, 1997). Our 'belt' model for discoidal HDL has received independent confirmation from solution-phase polarized internal reflection infrared spectroscopy experiments on oriented apo A-I and apo Δ(1–43)A-I discoidal lipoprotein complexes (Koppaka *et al.*, 1999).

Here, we report experimental details on the crystallization and 4 Å structure determination of apo Δ(1–43)A-I. These crystals exhibit several unusual diffraction characteristics, which are explained here in the context of the known crystal structure (Borhani *et al.*, 1997). Work to extend the diffraction data to higher resolution, through the use of cryogenic data collection at synchrotron-radiation sources, is also described.

2. Materials and methods

2.1. Crystallization

Recombinant human apoA-I [residues 44–243, plus a vector-derived N-terminal methionine, 'apo Δ(1–43)A-I', molecular weight 23 264 Da] was overexpressed and purified as described by Rogers *et al.* (1997). Determination of the purity of the stored protein, the concentration of the protein and preliminary crystallization screens were carried out as described by Borhani *et al.* (1999). Two crystal forms were obtained: form I is described below; form II crystals, which grow from polyethylene glycol 4000, 0.5 *M* NaOAc pH 7.5–8.75 containing 0.25%(*w*/*v*) β-D-octylglucopyranoside, are discussed in detail by Borhani *et al.* (1999).

2.1.1. Crystal form I. 5 µl of apo Δ(1–43)A-I was mixed with an equal volume of precipitant solution (1.0–1.4 *M* sodium citrate, 1.2–1.5 *M* potassium citrate or 1.4 *M* sodium potassium tartrate, buffered with 100 m*M* Na MES pH 6.5 or 100 m*M* Na HEPES pH 7.5). The mixture was allowed to equilibrate at 277 K as a hanging drop on siliconized (Aqua-Sil, Pierce) glass cover slips over 1 ml of the precipitant solution (in 24-well Linbro plastic tissue-culture plates). Large bipyramidal crystals appeared in one week and grew to maximum dimensions of 800 × 600 × 600 µm in 3–6 weeks. The crystals usually grew in the presence of large amounts of precipitated protein. Crystals could be harvested into an artificial mother liquor consisting of 8 volumes of 1.8 *M* sodium citrate, 0.5 volumes of 2.0 *M* Na HEPES pH 7.5 and 1.5 volumes of H_2O (final pH ∼7.65 at 277 K), in which they were stable indefinitely.

2.1.2. Crystal density measurement. The density of the crystals as a function of mother-liquor density was determined according to Colman & Matthews (1971), using an improved procedure for flotation in a calibrated ethylbenzene/iodobenzene density-gradient column (Leung *et al.*, 1999). The mother-liquor density was varied from 1.1929 to 1.7488 g ml^{-1} by mixing 3.5 *M* Cs_2SO_4, 1.8 *M* sodium citrate and 3.0 *M* potassium citrate with H_2O. Crystals equilibrated (277 K, 18 h) in these mother liquors had densities ranging from 1.2513 to 1.6816 g ml^{-1}.

2.2. X-ray diffraction analysis

2.2.1. Laboratory. Crystals were harvested either directly from the growth droplet or from the artificial mother liquor and mounted in thin-walled glass capillaries (1.0 mm diameter). X-ray diffraction data were collected at 282 K (forced-air apparatus) on a Siemens SRA rotating-anode generator (50 kV, 108 mA, graphite-monochromated Cu $K\alpha$ radiation) equipped with a MAR Research image-plate detector. Diffraction data were collected by the rotation method (typically 1.0° rotation per frame, 7.5 min each) and were processed with the *CCP*4 suite of programs (Collaborative Computational Project, Number 4, 1994). After determining the crystal orientations with *REFIX* (Kabsch, 1993) and *IDXREF*, the data were integrated with *MOSFLM* (Leslie, 1992). Weak higher resolution data were removed with *BATCH_CUTOFF*, an in-house program that applies a batch-wise resolution-dependent cut-off [all data in a batch beyond resolution d removed when $\langle I/\sigma_I \rangle$ is less than a cut-off value (typically 2.5) in resolution shell d]. The trimmed data were scaled and merged with *SCALA* (Evans, 1997) and placed on an absolute scale with *TRUNCATE* (French & Wilson, 1978). Precession photographs were obtained with Ni-filtered Cu $K\alpha$ radiation (0.2 mm collimator) at 282 K.

2.2.2. Synchrotron. The crystals were equilibrated in their artificial mother liquor and then passed through mother liquors supplemented with 10, 20 and 30%(*w*/*v*) glucose or sucrose (5 min in 10 and 20%, 15 min in 30%). Crystals were mounted in rayon loops (Hampton Research) and flash-cooled by plunging into liquid nitrogen. The crystals tolerated this protocol well, remaining optically clear throughout. Data were collected at the Cornell High Energy Synchrotron Source (beamline A1, λ = 0.908 Å, ADSC Quantum-1 CCD detector) and the National Synchrotron Light Source (beamline X25, λ = 1.100 Å, Brandeis B4 CCD detector) by the rotation method (0.5–1.0°, typically 60 s exposure) at 100 K. Data were processed as described above, except that no cut-off was used. Some exploratory data were also collected at the Stanford Synchrotron Radiation Laboratory (beamline 7-1, λ = 1.080 Å, MAR Research image-plate detector) at 277 K.

2.2.3. Rotation function. The self-rotation function was calculated in polar angles with *GLRF* (Tong & Rossmann, 1990), using data between 20 and 4.5 Å resolution. The Patterson integration radius was 35 Å and the Patterson origin was removed. The AXABZ orthogonalization convention was used (equivalent to NCODE = 1 in *AMoRe*, namely a on x, c^* on z); polar angle ψ is the angle between the rotation axis and the z axis, φ is the angle between the projection of this rotation axis onto the ab plane and the a axis and κ is the rotation angle about this axis. Confirmation of the polar angle self-rotation function results was obtained in Eulerian angles with *AMoRe* (Navaza, 1994). The same parameters were used in the calculation; Bessel orders lower than 6 were not used.

2.2.4. Phasing. Crystals were soaked in artificial mother liquor containing 1 m*M* $[Pt_2I_2en_2](NO_3)_2$ (PIP; Strem Chemical) for 4 and 39 h. Diffraction data were collected in the laboratory as described above. For the two crystals soaked

for 39 h, a crystallographic twofold screw axis was aligned parallel to the spindle in order to optimize collection of the anomalous scattering data. Heavy-atom sites were identified on the Harker sections of origin-removed difference Patterson maps; sites were confirmed with the automated search procedure *HASSP* (Terwilliger *et al.*, 1987). Heavy-atom parameters were refined with *HEAVY* (Terwilliger & Eisenberg, 1983), which was also used to calculate phases. Solvent flattening and non-crystallographic symmetry averaging were carried out with *DM* (Cowtan, 1994).

3. Results and discussion

3.1. Crystallization of apo Δ(1–43)A-I

The *N*-terminal truncation mutant of human apo A-I, apo Δ(1–43)A-I, crystallized at 277 K from sodium citrate, potassium citrate or sodium potassium tartrate pH 6.5–7.5. These crystals (form I) often grew in the presence of precipitated protein and reached maximum dimensions of 800 × 600 × 600 µm in a few weeks. The bipyramidal crystals usually possessed clean morphology with sharp edges. Sometimes the crystals grew with concave curved edges. The X-ray diffraction characteristics of these two morphological variants were indistinguishable. The form I crystals did not grow in the presence of β-D-octylglucopyranoside, whereas form II crystals, described in Borhani *et al.* (1999), grew only in its presence.

The apo Δ(1–43)A-I form I crystals were extremely sensitive to thermal damage and X-ray-induced radiation damage. Without cooling, no diffraction data could be collected. With cooling to 282 K, however, the crystals diffracted X-rays strongly to 7 Å resolution and weakly to ∼3.8 Å on a rotating-anode generator. Even with cooling, however, useful data could be collected for only several hours; data beyond 7 Å could be collected for only the first few hours of X-ray exposure. Precession photographs of the three zero-layers (Fig. 1) showed that apo Δ(1–43)A-I had crystallized in space group $P2_12_12_1$, with unit-cell parameters a = 97.47, b = 113.87, c = 196.19 Å. The unit-cell volume, 2 177 495 Å^3, was consistent with the presence of 4–12 molecules in the asymmetric unit (V_M = 5.85–1.95 Å^3 Da^{-1}; 79–38% solvent).

Inspection of the precession photographs revealed two noteworthy features. Firstly, a characteristic 'X', or pair of intensity spikes, was present in centre of the (*h*0*l*) and (0*kl*) layers (Fig. 1). The spikes were oriented at ∼24° to the *h* or *k* axes. Secondly, the low-order *h*-axis reflections 6,0,0 and 10,0,0 were very strong, whereas reflections 2,0,0, 4,0,0 and 8,0,0 were very weak. Examination of the integrated *h*00 intensities showed that this pattern extended to higher resolution (12,0,0 weak; 14,0,0 strong). Additionally, the low-order *k*-axis reflection 0,8,0 was very strong, whereas reflections 0,2,0, 0,4,0 and 0,6,0 were quite weak.

3.2. Characterization of the apo Δ(1–43)A-I crystals

Because the large size of the apo Δ(1–43)A-I unit cell was consistent with wide limits on the number of molecules in the asymmetric unit, we thought it imperative to delineate the unit-cell contents through density measurements and calculation of the self-rotation function. The density of the crystals was measured as a function of variable mother-liquor density (Leung *et al.*, 1999). The crystal density, D_c, was found to be a linear function of the mother-liquor density, D_s, as expected

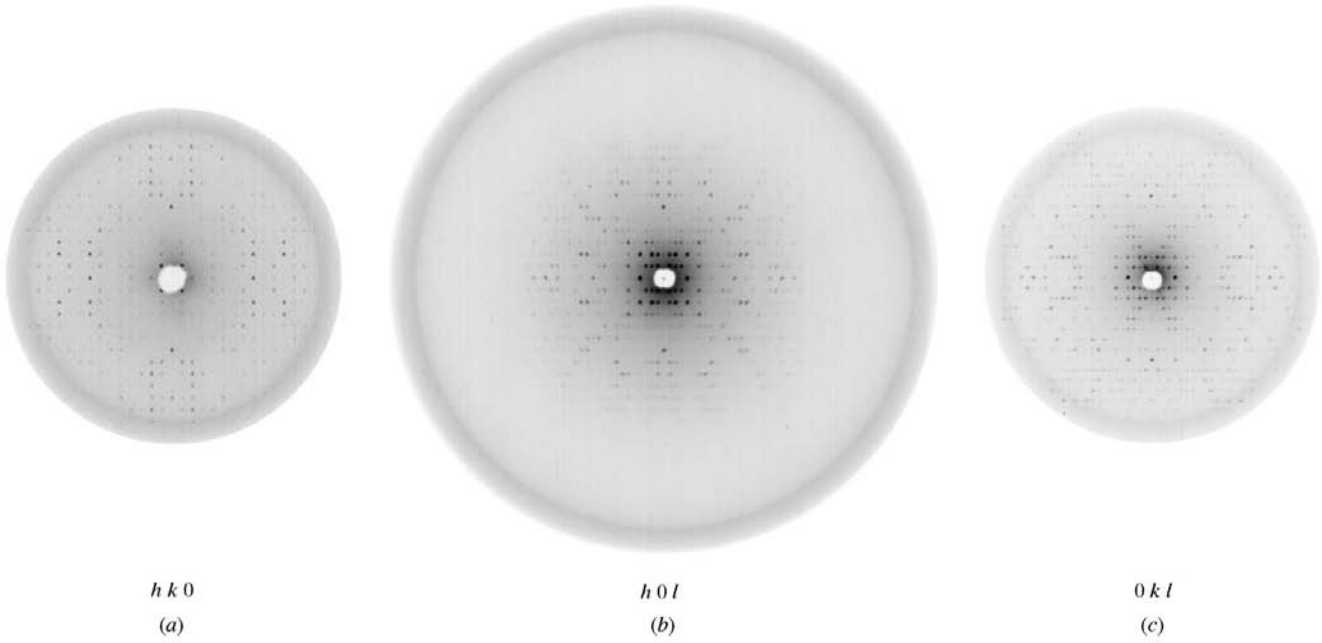

Figure 1
Precession photographs of the apo Δ(1–43)A-I crystals. (*a*) A 6° precession photograph of the (*hk*0) layer. The *h* axis is vertical; the *k* axis is horizontal. (*b*) A 10° precession photograph of the (*h*0*l*) layer. The *h* axis is vertical; the *l* axis is horizontal. (*c*) A 6° precession photograph of the (0*kl*) layer. The *k* axis is vertical; the *l* axis is horizontal.

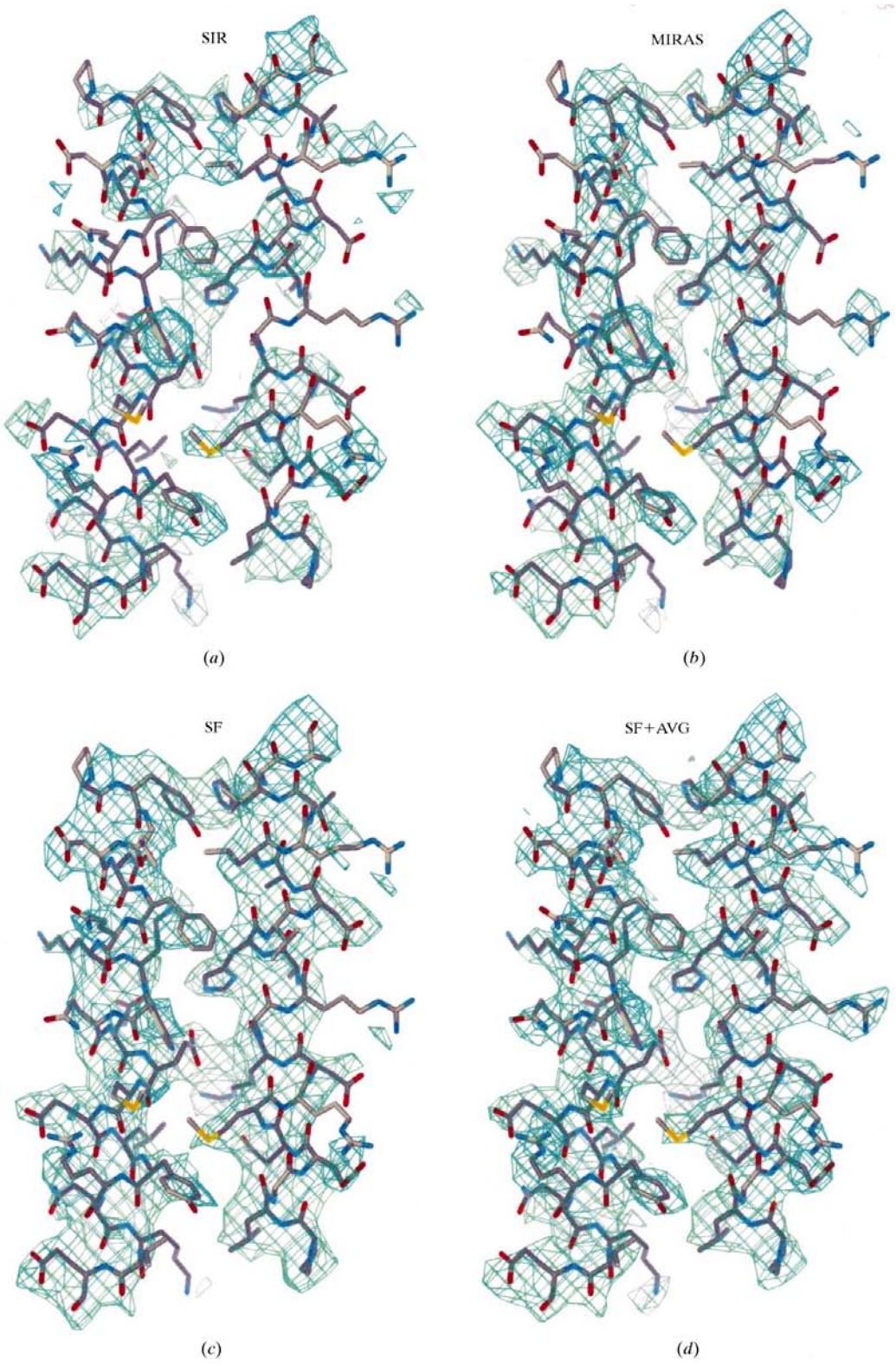

Figure 2
Electron-density maps at four stages of the apo Δ(1–43)A-I structure determination. Helices 4 (left; molecule *A*, residues 99–121) and 6 (right; molecule *B*, residues 143–164) of the refined 4 Å structure (Borhani *et al.*, 1997) are shown in each panel (grey, carbon; blue, nitrogen; red, oxygen; yellow, sulfur). The Pt ligands Met112 and Met148 are present in these helices and helix 4 also has an uniquely high number of aromatic residues (from top to bottom: Tyr100, Phe104, Trp108 and Tyr115). The (*a*) 4.5 Å SIR, (*b*) 4.5 Å MIRAS, (*c*) 4 Å solvent-flattened and (*d*) final 4 Å sharpened solvent-flattened twofold non-crystallographic symmetry averaged maps are contoured at 1σ; phases from the model were not used in the generation of any of these maps.

(Colman & Matthews, 1971): $D_c = 0.333 + 0.749D_s$. From this relationship, the volume percentages of protein, bound water and freely exchangeable solvent in the apo Δ(1–43)A-I unit cell were determined to be 22, 3 and 75%, respectively. The number of apo Δ(1–43)A-I molecules in the asymmetric unit was also thereby determined to be 4.24, *i.e.* 4 (Leung *et al.*, 1999).

To define the non-crystallographic symmetry, the self-rotation function (SRF) was calculated using data collected from two crystals at 282 K. Two strong peaks (both 47% of the height of the crystallographic twofold axes along *a, b* and *c*) were observed at polar angles (ψ, φ, κ) = (0, 0, 90°) and (90, 44, 180°). These peaks indicated, respectively, the presence of either a non-crystallographic fourfold axis parallel to the *c* axis or a twofold axis in the *ab* plane, halfway between the *a* and *b* axes. We called this twofold axis '*A*/*C*' for reasons explained below. In general, combination of a non-crystallographic twofold axis with a crystallographic twofold (screw) axis always generates another non-crystallographic (screw) axis of rotation angle 2δ (where δ is the angle between the two twofold axes), perpendicular to the plane defined by the two twofold axes. Details are provided in *Appendix A*. Since in this particular case the non-crystallographic twofold axis was 44° away from *a* in the *ab* plane, an 88° rotation (*i.e.* a fourfold axis) along *c* was generated. In the absence of other information, it was not possible to distinguish whether the fourfold or the twofold axis or both represented the true non-

crystallographic symmetry present in the asymmetric unit.

The apparent presence of a non-crystallographic fourfold axis parallel to *c* was reinforced by examination of both the (*hkn*) layers and low-order 00*l* reflections. As shown in Fig. 1, the (*hk*0) layer exhibited fourfold pseudosymmetry in the broad outlines of where the molecular transform was strong *versus* weak, a pattern shared by the other low-resolution (*hkn*) layers. Additionally, reflections 0,0,4, 0,0,8 and 0,0,12 were much stronger than adjacent 00*l* reflections, which suggested the presence of a non-crystallographic 4_1 or 4_3 screw axis parallel to *c*. This extinction pattern was not absolute, however, and it broke down completely after 0,0,12.

The ambiguity in the non-crystallographic symmetry was partly resolved by the observation of two additional peaks in the SRF at (ψ, φ, κ) = (112, 308, 180°) (height 26%, '*A*/*B*') and (158, 132, 180°) (height 16%, '*A*/*D*'). These weak twofold axes, when combined with the strong non-crystallographic twofold axis '*A*/*C*', yielded a self-consistent set of mutually perpendicular twofold rotation axes. This result suggested that the asymmetric unit contained four molecules of apo Δ(1–43)A-I arranged as a 222-symmetrical tetramer. We tentatively concluded that the apparent fourfold non-crystallographic symmetry was purely a result of the combination of a crystallographic twofold screw axis with the non-crystallographic twofold axis in the *ab* plane, which was located by chance 44° away from the *a* axis.

3.3. Heavy-atom derivatization and structure determination

At this point, data were collected from a crystal soaked with $[Pt_2I_2en_2](NO_3)_2$ (PIP) for 4 h. Visual inspection of the difference Patterson map revealed a single site, consistent with all three Harker sections, at fractional coordinates (0.557, −0.211, −0.021). A Fourier map calculated with SIR phases (figure of merit = 0.29) revealed large diamond-shaped solvent regions delineated by rod-shaped protein regions. The rods were oriented at ±24° to the *c* axis. We immediately made the connection between the spikes in the diffraction pattern (Fig. 1), which arise from the constructive interference of paired α-helices aligned ±24° to *c* (see §3.4), and the rod-shaped density in the SIR map. A portion of the SIR map is shown in Fig. 2(*a*). Using data collected from two crystals soaked with PIP for 39 h, the first site and three additional sites were identified. The choice of hand for the heavy-atom model was obvious from SIRAS maps: the correct hand (chosen by chance initially) showed large solvent cavities (consistent with the 75% solvent content), whereas the incorrect hand produced a map in which the protein and solvent regions were interchanged. MIRAS phases were improved by several rounds of solvent flattening, such that difference Fourier maps now revealed a total of six sites for the 4 h soak and a seventh minor site for the 39 h soak. Refinement of the heavy-atom parameters gave a figure of merit of 0.50, with phasing powers of 1.32 (0.37 anomalous) and 1.23 (0.27) for the 39 and 4 h soaks, respectively. The MIRAS map (Fig. 2*b*) was improved by solvent-flattening (72% solvent). This map (Fig. 2*c*) showed large solvent

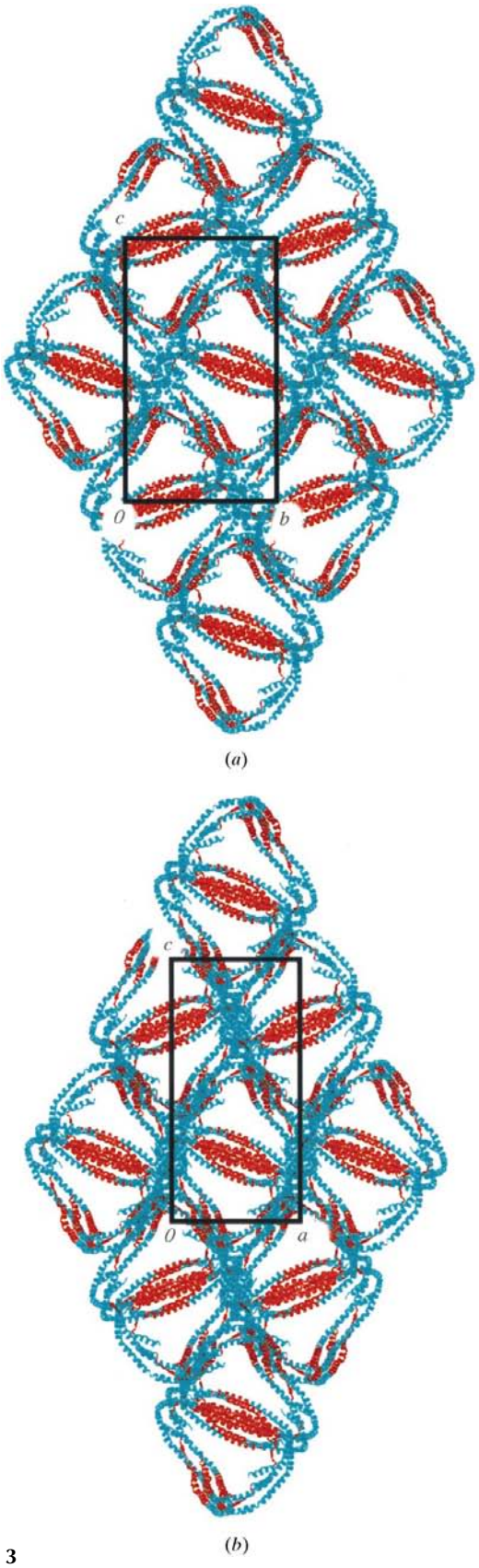

Figure 3
Experimentally determined molecular packing in the apo Δ(1–43)A-I crystals. (*a*) Projection along the *a* axis. (*b*) Projection along the *b* axis. Less-mobile parts of the apo Δ(1–43)A-I tetramers (B < 120 Å^2) are coloured cyan; more mobile regions are coloured red. The unit cell is shown in black.

Table 1
Apo Δ(1–43)A-I heavy-atom sites.

Site	Occupancy	Fractional coordinates†			Pt ligand	Related to site	By SRF peak‡
		x	*y*	*z*			
1	0.83	0.1466	0.5704	0.1578	Met *C*112	3	*A*/*B*
						5	*A*/*C*
						7	*A*/*D*
2	1.41	0.0887	0.5794	0.1334	Met *D*148	4	*A*/*B*
						6	*A*/*C*
						'8'	*A*/*D*
3	0.83	−0.0089	0.3393	0.2851	Met *D*112	5	*A*/*D*
						7	*A*/*C*
4	0.39	0.0046	0.3545	0.3146	Met *C*148	6	*A*/*D*
						'8'	*A*/*C*
5	0.84	0.8371	−0.0593	0.0936	Met *A*112	7	*A*/*B*
6	0.83	0.8520	−0.1188	0.1130	Met *B*148	'8'	*A*/*B*
7	1.25	0.5641	−0.2081	−0.0247	Met *B*112		
'8'	0§	0.5779 §	−0.1877§	−0.0632§	Met *A*148		

† Refined fractional coordinates and occupancies are shown for the 39 h PIP soak. The 4 h PIP soak lacked site 4 and had different relative occupancies for the other sites. ‡ Self-rotation function peak *A*/*B*, (ψ, φ, κ) = (112, 308, 180°), rotates molecules *A* and *C* onto molecules *B* and *D*, respectively. Similarly, SRF peak *A*/*C*, (90, 44, 180°), rotates *A* and *B* onto *C* and *D*, and SRF peak *A*/*D*, (158, 132, 180°), rotates *A* and *B* onto *D* and *C*. These rotation axes intersect (within 1 Å) in the centre of the apo Δ(1–43)A-I tetramer at fractional coordinates (0.3976, 0.1746, 0.1277). § PIP binding at site '8' was not detected experimentally. It is included here solely to clarify the non-crystallographic symmetry relationships among the seven observed Pt sites. These fractional coordinates are those of Met*A*148 SD in the refined model, PDB entry 1av1.

cavities surrounded by long tubes of density that curved throughout the unit cell. It was quite difficult to interpret this map, however, because no single asymmetric unit of the $P2_12_12_1$ unit cell contained more than one-sixth of an apo Δ(1–43)A-I molecule.

The refined coordinates and occupancies of the seven Pt sites are shown in Table 1. Upon inspection of these sites using molecular graphics (*O*; Jones *et al.*, 1991), it became clear that (i) the sites were grouped into pairs, except for site 7, which lacked its corresponding site '8', and (ii) the sites were related by the non-crystallographic 222 point symmetry described above [rotation axes centred at fractional coordinates (0.3976, 0.1746, 0.1277)]. The strong twofold axis, which we later named '*A*/*C*' (see below), rotated sites 1 and 2 onto sites 5 and 6, respectively, and sites 3 and 4 onto sites 7 and '8'. A natural consequence of the non-crystallographic 222 point symmetry was that the weak twofold axes, '*A*/*B*' and '*A*/*D*', also rotated the Pt sites onto one another.

With a clear understanding of the non-crystallographic symmetry, it was now possible to interpret the solvent-flattened map in terms of four horseshoe-shaped pseudo-continuous α-helices associated together in the shape of a ring. Molecules *A* and *B* of the tetramer, which had very similar but distinct shapes, were related to molecules *C* and *D* by application of the strong *A*/*C* non-crystallographic twofold axis. The *A*/*B* and *A*/*D* twofold axes were much weaker in the SRF because these molecules were related by approximate rather than exact symmetry. A C^{α} chain trace was built into the solvent-flattened map (Fig. 2*c*) and this model was used to construct an averaging mask around the *A*/*B* dimer. The map was then subjected to twofold non-crystallographic symmetry averaging about the *A*/*C* axis. Assignment of the seven Pt ligands as methionine residues 112 and 148 in each of the four apo Δ(1–43)A-I chains in the asymmetric unit (except Met A148, site '8'; Table 1), the realisation that the high aromatic residue content of helix 4 (residues 99–121) was unique in the apo A-I sequence and the observation of kinks in the electron density for each of the seven prolines in apo Δ(1–43)A-I allowed the chain trace to be completed. Application of a sharpening artificial temperature factor (−70 $Å^2$; Stehle *et al.*, 1996) followed by additional symmetry averaging provided the final map (Fig. 2*d*), in which many protein side chains were visible (Borhani *et al.*, 1997).

3.4. Unusual X-ray diffraction characteristics of the apo Δ(1–43)A-I crystals

3.4.1. Spikes. Diffraction spikes, which are characteristic of a strong molecular repeat in a perpendicular direction in the unit cell, are usually observed only in fibrous (*e.g.* tropomyosin α-helical coiled coils) or spherically symmetrical (*e.g.* viruses; Caspar, 1956) molecules. In fact, the spikes observed from apo Δ(1–43)A-I crystals (Fig. 1) are very similar to those observed from tropomyosin crystals (Cohen *et al.*, 1972; Phillips *et al.*, 1980), which consist of coiled coils running along the body diagonal of the unit cell (Phillips *et al.*, 1980). These X-ray data indicated to us that apo Δ(1–43)A-I had crystallized as a monomer or multimer that consisted of closely apposed parallel or antiparallel α-helices. Examination of a packing diagram (Fig. 3) shows that the better ordered portions of the tetrameric apo Δ(1–43)A-I ring (helices 4–6 and 10) are aligned at ±24° to the *c* axis. Only these portions of apo Δ(1–43)A-I were apparent in the first SIR map. Diffraction spikes from other parts of the structure, *e.g.* helices 1–3 and 7–9, are not observed because these regions of the molecule are more mobile, as reflected by their higher temperature factors. Since we understood the origin of the diffraction spikes before obtaining the PIP derivative, we were sufficiently encouraged by the SIR map to use this single derivative to solve the structure.

3.4.2. Axial reflections. The axial reflections of the apo Δ(1–43)A-I crystals are very unusual (see §3.1 and Fig. 1). We felt that it was important to understand the origin of these unusual diffraction effects. Although our analysis did not ultimately help to solve this structure, it may prove helpful to others as a didactic tool.

3.4.3. *h* axis. The Fourier representation of an electron-density square wave (density = +1, x = 0–0.25*a*; −1, 0.25*a*–0.5*a*; +1, 0.5*a*–0.75*a*; −1, 0.75*a*–*a*) has spatial frequency components (*h* indices) of order 1, 3, 5, 7, ..., only. If the spatial periodicity of the square wave is doubled (*i.e.* density = +1, x = 0–0.125*a*; −1, 0.125*a*–0.25*a*, *etc.*), the allowed frequency

Table 2
Fourier analysis of the apo Δ(1–43)A-I crystals' *a*-axis projection electron-density.

h index	$\lvert F_{obs}\rvert$†	φ_{obs}‡	Fourier coefficient F_h	
			Experimental projection electron-density†	Step-function approximation†
2	NM§	ND§	+0.1	+10.0
4	NM§	ND§	−0.1	+8.8
6	100.0	−	−100.0	−100.0
8	9.0	−	−6.2	+15.4
10	73.5	+	+72.0	+78.7
12	10.5	+	+10.1	−10.7
14	32.9	−	−30.9	−22.8

† Normalized to set value of reflection 6,0,0 equal to 100. ‡ Experimental phases from inverse Fourier transformation of the solvent-flattened symmetry-averaged MIRAS map. § NM, not integrated, but very weak (see Fig. 1); ND, not determined.

components (*h* indices) become 2, 6, 10, 14, ... These *h* indices (except 2) correspond to just those strong *h*00 reflections observed from the apo Δ(1–43)A-I crystals. Therefore, the molecules must be packed in such a way that at low resolution (*i.e.* less than 97.47 Å/14 $\simeq$ 7 Å) the projection of electron density along the crystallographic *a* axis from $x = 0$–$0.5a$ has an 'up–down–up–down' appearance. This appearance must be somewhat distorted, however, in order to weaken the 2,0,0 reflection.

Shown in Fig. 4 is the *a*-axis projection electron density of the apo Δ(1–43)A-I crystals (4 Å resolution; Borhani *et al.*, 1997). Also shown is a step-function approximation, $f(x)$, to this density. This step function has the distorted 'up–down–up–down shape, as well as the same symmetry as the one-dimensional $P2_12_12_1$ projection (line group *pm*). Fourier series analysis of this step function provided normalized Fourier coefficients (structure factors), F_h. These are shown in Table 2 along with those F_h obtained by Fourier series analysis of the projection electron density itself. It can be seen that this simple step-function approximation to the observed apo Δ(1–43)A-I *a*-axis projection electron density replicates fairly well the strong 6,0,0, 10,0,0 and 14,0,0 reflections, coupled with weak 2,0,0, 4,0,0, 8,0,0 and 12,0,0 reflections. Upon modification of the step function $f(x)$ to remove the small hump in the centre, F_h for the 2,0,0 reflection became much stronger, comparable to that for 6,0,0 and 10,0,0. Therefore, this hump is the distortion of the 'up–down–up–down' pattern mentioned above.

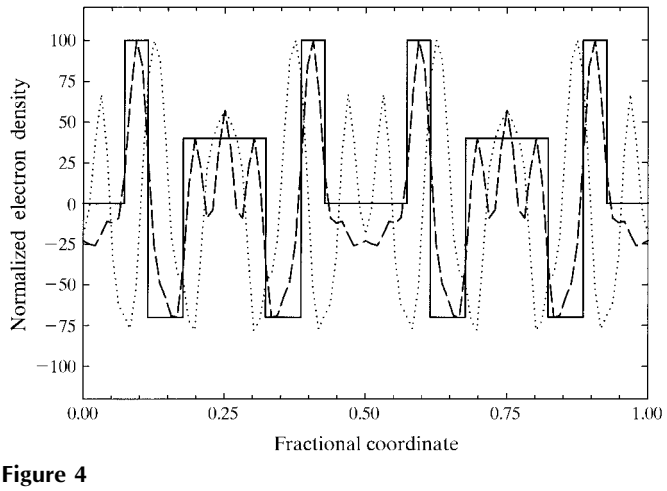

Figure 4
Axial projection electron density of the apo Δ(1–43)A-I crystals. The abscissa represents fractional coordinates 0–1 and the ordinate represents the electron density. Broken line, normalized experimental electron density (derived from the final 4 Å experimental map; Borhani *et al.*, 1997) projected along the *a* axis. Unbroken line, square-wave approximation, $f(x)$, to the *a*-axis projection electron density (see text). $f(x) = 0$ for $x = 0.000$–0.076 and 0.424–0.500; $f(x) = +100$ for $x = 0.076$–0.125 and 0.375–0.424; $f(x) = -70$ for $x = 0.125$–0.186 and 0.314–0.375; $f(x) = +40$ for $x = 0.186$–0.314. Dotted line, normalized experimental electron density projected along the *b* axis.

3.4.4. *k* axis. Reflection 0,8,0 is the first strong *k*-axis reflection; the others are extremely weak. Simple considerations suggest, therefore, that the *b*-axis projection electron density must approximate the function $\sin(2\pi 8y)$, *i.e.* a Fourier synthesis would have order $k = 8$ as its lowest frequency component. Indeed, the *b*-axis projection electron density, also shown in Fig. 4, has this shape.

3.5. Diffraction characteristics of flash-cooled crystals

We examined whether cryogenic data collection could improve the poor diffraction characteristics of the apo Δ(1–43)A-I crystals. Several cryoprotectants were tested. Glycerol, ethylene glycol and PEG 400 all failed to protect these crystals from becoming disordered upon cooling to cryogenic temperatures. The crystals tolerated a mother liquor supplemented with 30% glucose or sucrose, however, and could then be successfully flash-cooled in liquid nitrogen. Flash-cooled apo Δ(1–43)A-I crystals diffracted synchrotron radiation to 3 Å resolution. The crystals remained quite sensitive even at 100 K, however, with the diffraction limit falling back to 4 Å after about 20–30 min. Efforts to assemble a complete 3 Å data set from several crystals have been hampered by a subtle crystal-to-crystal variation that occurs upon flash-cooling. This variation is likely to be related to the shrinkage of the unit cell upon flash-cooling ($a = 94.56$, $b = 113.36$, $c = 194.16$ Å) and to the motion of the molecules in the crystals, which gives rise to diffuse scattering effects at room temperature (data not shown).

We were able to collect a complete data set from one unusually stable crystal, however, for the limited resolution range 100–3.46 Å. The overall R_{sym} for these data is 6.8% (36.6% for data in the 3.57–3.46 Å shell), $\langle I/\sigma_I\rangle$ is 11.0 (3.6), the completeness is 96.6% (99.6%) and the mean multiplicity is 4.0 (3.8). As the first step of 3.5 Å refinement, we used the experimental 4 Å room-temperature electron-density map as a molecular-replacement search model for the flash-cooled structure. The resulting 4 Å phases were improved and extended to 3.5 Å by solvent flattening (no NCS averaging or artificial temperature factor sharpening). Examination of the new electron-density map shows that our original atomic model for apo Δ(1–43)A-I is correct in the main and that several detailed features of our model (*e.g.* the helix–helix

interactions) are also correct. Refinement at 3.5 Å will be reported elsewhere.

Finally, several options are being explored to stabilize the crystals against radiation damage so that their full 3.0 Å potential can be realised. These options include optimization of the cryobuffer and the flash-cooling protocol, the inclusion of metal ions to stabilize the crystal lattice (Chang *et al.*, 1998) and data collection at much lower temperatures (*e.g.* 30 K).

APPENDIX *A*

Without loss of generality, take a crystallographic twofold rotation axis along the x axis (rotation matrix $\mathbf{2_x}$) and another, non-crystallographic, twofold rotation axis δ degrees away from x toward y in the xy plane (rotation matrix $\mathbf{2}_\delta$). We show here that the combination of these two rotations generates a third rotation, $\mathbf{R}_\mathbf{z}^{2\delta}$, of magnitude 2δ perpendicular to the plane defined by the twofold axes.

Let rotation around the z axis by angles δ and $-\delta$ be represented by matrices $\mathbf{R}_\mathbf{z}^{\delta}$ and $\mathbf{R}_\mathbf{z}^{\bar{\delta}}$, respectively. Matrix $\mathbf{2}_\delta$ is therefore defined as

$$\mathbf{2}_\delta = \mathbf{R}_\mathbf{z}^{\delta}\mathbf{2_x}\mathbf{R}_\mathbf{z}^{\bar{\delta}} = \begin{pmatrix} \cos\delta & \overline{\sin\delta} & 0 \\ \sin\delta & \cos\delta & 0 \\ 0 & 0 & 1 \end{pmatrix}\begin{pmatrix} 1 & 0 & 0 \\ 0 & \bar{1} & 0 \\ 0 & 0 & \bar{1} \end{pmatrix}\begin{pmatrix} \cos\delta & \sin\delta & 0 \\ \overline{\sin\delta} & \cos\delta & 0 \\ 0 & 0 & 1 \end{pmatrix}.$$

Carrying out the matrix multiplication yields the following result:

$$\mathbf{2}_\delta = \begin{pmatrix} \cos\delta\cos\delta - \sin\delta\sin\delta & 2\cos\delta\sin\delta & 0 \\ 2\cos\delta\sin\delta & \sin\delta\sin\delta - \cos\delta\cos\delta & 0 \\ 0 & 0 & \bar{1} \end{pmatrix} = \begin{pmatrix} \cos 2\delta & \sin 2\delta & 0 \\ \sin 2\delta & \overline{\cos 2\delta} & 0 \\ 0 & 0 & \bar{1} \end{pmatrix}.$$

Finally, combination of $\mathbf{2_x}$ with $\mathbf{2}_\delta$ gives

$$\mathbf{2}_\delta\mathbf{2_x} = \begin{pmatrix} \cos 2\delta & \sin 2\delta & 0 \\ \sin 2\delta & \overline{\cos 2\delta} & 0 \\ 0 & 0 & \bar{1} \end{pmatrix}\begin{pmatrix} 1 & 0 & 0 \\ 0 & \bar{1} & 0 \\ 0 & 0 & \bar{1} \end{pmatrix} = \begin{pmatrix} \cos 2\delta & \overline{\sin 2\delta} & 0 \\ \sin 2\delta & \cos 2\delta & 0 \\ 0 & 0 & 1 \end{pmatrix} = \mathbf{R}_\mathbf{z}^{2\delta}.$$

Matrix $\mathbf{R}_\mathbf{z}^{2\delta}$ describes a rotation around the z axis by an angle 2δ. In general, the matrix product $\mathbf{2}_\delta\mathbf{2_x}$ does not commute with $\mathbf{2_x}\mathbf{2}_\delta$, which describes a rotation ($\mathbf{R}_\mathbf{z}^{\bar{2\delta}}$) around the z axis by an angle -2δ. (The matrices commute only if $2\delta = 180°$.)

Usually, we ignore the peaks in the self-rotation function arising from $\mathbf{R}_\mathbf{z}^{2\delta}$ and $\mathbf{R}_\mathbf{z}^{\bar{2\delta}}$, because the angle δ between the non-crystallographic and crystallographic twofold rotation axes is random and thus the rotations $\mathbf{R}_\mathbf{z}^{2\delta}$ and $\mathbf{R}_\mathbf{z}^{\bar{2\delta}}$ do not correspond to an 'expected' arrangement of protomers in the asymmetric unit. If the angle δ is 'special', however, *e.g.* 30, 36, 45, 60 or 90°, then the generated non-crystallographic rotation axes correspond to a rotation of 60, 72, 90, 120 or 180°, respectively, around z, *i.e.* a six-, five-, four-, three- or twofold rotation axis, respectively.

We thank Danise Rogers, Margie Ray and Larry Ross for assistance with production of recombinant apo Δ(1–43)A-I and Annie Héroux for help with some of the synchrotron data collection. We are also grateful for the assistance of Dan Thiel (Cornell High Energy Synchrotron Source), Mike Soltis (Stanford Synchrotron Radiation Laboratory) and Bob Sweet (National Synchrotron Light Source). We thank Bill Stallings for very helpful comments on the manuscript. DWB is an Established Investigator of the American Heart Association (Grant No. 974008N). This work was also supported by Southern Research Institute (Project Nos. 1008 and 1026). Finally, DWB is deeply grateful to his wife, Julie Bernstein, for her cheerful and tireless support.

References

Acton, S., Rigotti, A., Landschulz, K. T., Xu, S., Hobbs, H. H. & Krieger, M. (1993). *Science*, **271**, 518–520.
Borhani, D. W., Engler, J. A. & Brouillette, C. G. (1999). *Acta Cryst.* D**55**, 1578–1583.
Borhani, D. W., Rogers, D. P., Engler, J. A. & Brouillette, C. G. (1997). *Proc. Natl Acad. Sci. USA*, **94**, 12291–12296.
Caspar, D. L. D (1956). *Nature (London)*, **177**, 475–476.
Castelli, W. P., Garrison, R. J., Wilson, P. W. F., Abbott, R. D., Kalousdian, S. & Kannel, W. B. (1986). *J. Am. Med. Assoc.* **256**, 2835–2838.
Catapano, A., Bernini, F. & Corsini, A. (1993). Editors. *Atherosclerosis Reviews*, Vol. 24, *High-Density Lipoproteins: Physiopathology and Clinical Relevance.* New York: Raven.
Chang, C., Spencer, R. H., Lee, A. T., Barclay, M. T. & Rees, D. C. (1998). *Science*, **282**, 2220–2226.
Cohen, C., Caspar, D. L. D., Parray, D. A. D. & Lucas, R. M. (1972). *Cold Spring Harbor Symp. Quant. Biol.* **36**, 205–216.
Collaborative Computational Project, Number 4 (1994). *Acta Cryst.* D**50**, 760–763.
Colman, P. M. & Matthews, B. W. (1971). *J. Mol. Biol.* **60**, 163–168.
Cowtan, K. (1994). *Jnt CCP4–ESF/EACBM Newslett. Protein Crystallogr.* **31**, 34–38.
Evans, P. R. (1997). *Jnt CCP4–ESF/EACBM Newslett. Protein Crystallogr.* **33**, 22–24.
French, S. & Wilson, K. (1978). *Acta Cryst.* A**34**, 517–525.
Gordon, T., Castelli, W. P., Hjortland, M. C., Kannel, W. B. & Dawber, T. R. (1977). *Am. J. Med.* **62**, 707–714.
Jones, T. A., Zou, J. Y., Cowan, S. W. & Kjelgaard, M. (1991). *Acta Cryst.* A**47**, 110–119.
Kabsch, W. (1993). *J. Appl. Cryst.* **24**,795–800.
Koppaka, V., Silvestro, L., Engler, J. A., Brouillette, C. G. & Axelsen, P. H. (1999). *J. Biol. Chem.* **274**, 14541–14544.
Kozarsky, K. F., Donahee, M. H., Rigotti, A., Iqbal, S. N., Edelman, E. R. & Krieger, M. (1997). *Nature (London)*, **387**, 414–417.
Leslie, A. G. W. (1992). *Jnt CCP4–ESF/EACMB Newslett. Protein Crystallogr.* **26**.
Leung, A. K. W, Park, M. M. V. & Borhani, D. W. (1999). *J. Appl. Cryst.* **32**, 1006–1009.
Miller, N. E. (1989). Editor. *High-Density Lipoproteins, Reverse Cholesterol Transport and Coronary Heart Disease.* Amsterdam: Elsevier.

Miller, N. E., Førde, O. H., Thelle, D. S. & Mjøs, O. D. (1977). *Lancet*, **1**(8019), 964–968.
Navaza, J. (1994). *Acta Cryst.* A**50**, 157–163.
Phillips, G. N. Jr, Fillers, J. P. & Cohen, C. (1980). *Biophys. J.* **32**, 485–502.
Plump, A. S., Erickson, S. K., Weng, W., Partin, J. S., Breslow, J. L. & Williams, D. L. (1996). *J. Clin. Invest.* **97**, 2660–2671.
Rigotti, A., Trigatti, B. L., Penman, M., Rayburn, H., Herz, J. & Krieger, M. (1997). *Proc. Natl Acad. Sci. USA*, **94**, 12610–12615.
Rogers, D. P., Brouillette, C. G., Engler, J. A., Tendian, S. W., Roberts, L., Mishra, V. K., Anantharamaiah, G. M., Lund-Katz, S., Phillips, M. C. & Ray, M. J. (1997). *Biochemistry*, **36**, 288–300.
Rothblat, G. H., Mahlberg, F. H., Johnson, W. J. & Phillips, M. C. (1992). *J. Lipid Res.* **33**, 1091–1097.
Stehle, T., Gamblin, S. J., Yan, Y. & Harrison, S. C. (1996). *Structure*, **4,** 165–182.
Terwilliger, T. C. & Eisenberg, D. (1983). *Acta Cryst.* A**39**, 813–817.
Terwilliger, T. C., Kim, S.-H. & Eisenberg, D. (1987). *Acta Cryst.* A**43**, 1–5.
Tong, L. & Rossmann, M. G. (1990). *Acta Cryst.* A**46**, 783–792.